

# How Graph Neural Network Interatomic Potentials Extrapolate: Role of the message-passing algorithm

Sungwoo Kang\*

Computational Science Research Center, Korea Institute of Science and Technology (KIST),  
Seoul, 02792, Republic of Korea

\*Email: [sung.w.kang@kist.re.kr](mailto:sung.w.kang@kist.re.kr)

## ABSTRACT

Graph neural network interatomic potentials (GNN-IPs) are gaining significant attention due to their capability of learning from large datasets. Specifically, universal interatomic potentials based on GNN, usually trained with crystal geometries, often exhibit remarkable extrapolative behavior towards untrained domains, such as surfaces or amorphous configurations. However, the origin of this extrapolation capability is not well understood. This work provides a theoretical explanation of how GNN-IPs extrapolate to untrained geometries. First, we demonstrate that GNN-IPs can capture non-local electrostatic interactions through the message-passing algorithm, as evidenced by tests on a toy model and DFT data. We find that GNN-IPs accurately predict electrostatic forces in untrained domains, indicating that they have learned the exact functional form of the Coulomb interaction. Based on these results, we suggest that the ability to learn non-local electrostatic interactions, coupled with the embedding nature of GNN-IPs, explains their extrapolation ability.

Finally, we find that the universal GNN-IP, SevenNet-0, effectively infers non-local Coulomb interactions in untrained domains.

KEYWORDS: machine-learned potential, machine learning potential, machine learning force field, universal interatomic potential, foundation model, graph neural network

## 1. INTRODUCTION

Machine-learned interatomic potentials (MLIPs), which are machine learning models that predict the energies of given atomic configurations based on reference quantum mechanical calculation data, have gained much attention due to their speed, linear scalability, and high accuracy compared to density-functional theory (DFT) calculations.<sup>1</sup> Most early MLIP models predict the atomic energy of a given atom using input descriptors based on the local environment,<sup>2-4</sup> based on the assumption that non-local electrostatic interactions are effectively screened beyond a certain cutoff.<sup>5</sup> However, when it comes to systems involving large atomic charges, where electrostatic interactions are not screened within the cutoff radius, these conventional models fail to describe the potential energy surfaces (PES) of the system.<sup>6</sup> To overcome this issue, developments have been made to include non-local electrostatic interactions in conventional MLIPs.<sup>7-9</sup>

Recent developments in GNN-IPs have shown significant improvements in accuracy, data efficiency, and transferability compared to descriptor-based models.<sup>10-13</sup> These models incorporate a message-passing algorithm, suggesting their capability of extending the effective cutoff multiplied by the number of graph convolutions. However, it is still unclear whether these models effectively infer non-local electrostatics. Specifically, two previous studies explored this attribute

of GNN-IPs and reached conflicting conclusions: Bochkarev et al. demonstrated that GNN-IPs, specifically ml-ACE and NequIP models, effectively train on the PES of molecules longer than the cutoff distance with considerable partial charges, indicating their ability to learn electrostatic interactions.<sup>14</sup> However, the charge distribution of atoms within a molecule is coupled with structural deformation, making it unclear whether GNN-IPs primarily learn PES based on structural deformations or if they can directly learn electrostatic interactions independently of geometric coupling. Additionally, Nigam et al. showed that the message-passing algorithm can learn electrostatic interactions in random NaCl structures but concluded that this approach is much less effective compared to simply increasing the cutoff.<sup>15</sup> Specifically, they found that using the message-passing algorithm in linear models faces contradictory scenarios (see Figure 1a). However, it remains unknown how incorporating non-linearity would affect the results. For instance, including activation functions at nodes allows the information of atoms to be passed in a non-linear way (see Figure 1b), potentially capturing the correct electrostatic interactions regardless of atomic configurations. Overall, questions remain regarding the ability of GNN-IPs to model non-local electrostatic interactions effectively.

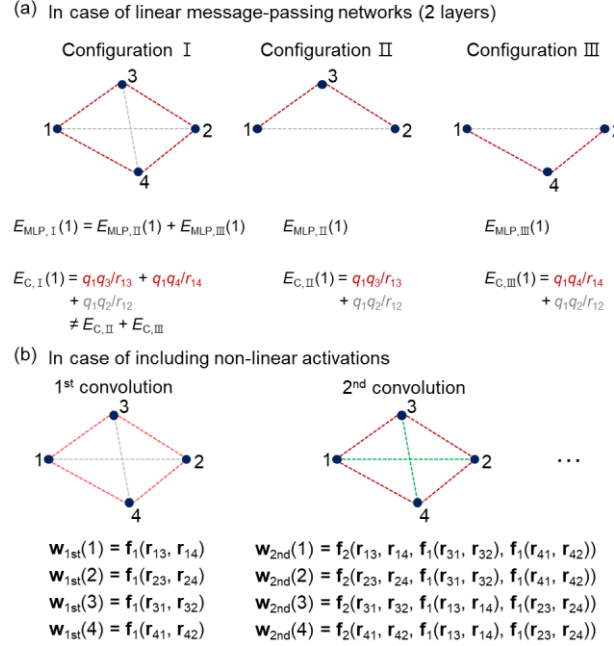


Figure 1. Schematic illustration of the message-passing algorithm for (a) a graph neural network with a linear activation function and (b) a non-linear activation function. In (a), the red lines indicate the message passing. The distances between nodes 1 and 2 ( $r_{12}$ ) and nodes 3 and 4 ( $r_{34}$ ) are assumed to be larger than the cutoff, so message passing does not occur within these pairs.  $E_{\text{MLP}}$  and  $E_{\text{C}}$  stand for the energy calculated from the MLIP and the reference Coulomb energy, respectively. In (b),  $\mathbf{w}_i$  is the feature value of the  $i$ -th layer, and  $\mathbf{f}$  denotes the network convolution function.

In addition to their ability to capture non-local interactions, GNN-IPs are attracting significant attention for their ability to learn a wide range of elemental systems. Utilizing this characteristic, they are often used to train universal interatomic potentials (UIPs) on massive databases (such as Materials Project<sup>16</sup>), enabling them to cover most elements in the periodic table.<sup>17–23</sup> These models demonstrate remarkable extrapolative capabilities in predicting properties across both untrained compositional and configurational spaces. As an example of compositional extrapolation, UIPs effectively predict the energy values of configurations in untrained compositions, such as novel-composition materials resulting from stoichiometric substitutions.<sup>20</sup> In the case of configuration extrapolation, although UIPs are primarily trained on crystal structure databases, they show a remarkable ability to predict properties such as phonon dispersion, Li diffusivity, structural

properties of amorphous phases, and even catalytic properties—though these predictions are not always highly accurate—for configurations not directly included in the training set.<sup>18-21</sup> It is suggested in ref.<sup>20</sup> that the use of atomic embedding is the origin of this extrapolation behavior because the knowledge learned from certain elemental systems can be transferred to other elemental systems. This transfer is possible because all elements share the same network structures and only differ by their embedding vectors. The embedding vectors are trainable, suggesting that the chemical relationships of elements are well represented in these vectors after training on a massive database. In this context, when visualizing the embedding vectors, it can be confirmed that elements with similar chemical properties are located close to each other.<sup>20</sup> Note that, in conventional descriptor-type models, this transfer is not feasible because the geometric information for elemental combinations is represented as separate descriptors, with distinct networks and weights used for different elements. This embedding characteristic of GNN-IPs explains their ability to extrapolate untrained compositions within the same configurations. However, it is still unclear how GNN-IPs accurately extrapolate to untrained configurations, such as amorphous structural orders.<sup>21</sup>

In this study, we demonstrate that GNN-IPs effectively capture electrostatic interactions, which explains their extrapolation ability in untrained configurations. The ability of GNN-IPs to learn non-local interactions is confirmed using a toy model consisting of randomly distributed charged particles. We find that the electrostatic interactions can be extrapolated within untrained ionic distances, indicating that GNN-IPs accurately learn electrostatic interactions. We also confirm that the electrostatic interactions and charge equilibrations can be described by GNN-IPs within DFT data, including the SrO crystal/disorder system and Au<sub>2</sub>-adsorbed undoped/doped MgO slab.

Finally, we provide a theoretical explanation of how GNN-IPs extrapolate to out-of-domain configurations using the extrapolative capability of non-local electrostatic interactions.

## **2. RESULTS**

### **2.1. Capability of learning electrostatic interactions**

Initially, we construct a simple toy model comprising particles with point charges, applying only electrostatic interactions. Figure 2a illustrates an example model used in this study. In the test simulations, we use pairs of structures (type I and II): In configuration type I, particles with charges of  $1e$ ,  $-1e$ ,  $0.5e$ , and  $-0.5e$  are included. The  $1e$  and  $-1e$  particles are placed at a specified distance ( $d$ ), while the  $0.5e$  and  $-0.5e$  particles are placed randomly in a non-periodic cell. Configuration type II is identical to type I but omits the  $-1e$  particle in each cell. (Note that in the training process, we also include type III configurations, which contain  $-1e$  particles but omit  $1e$  particles.)

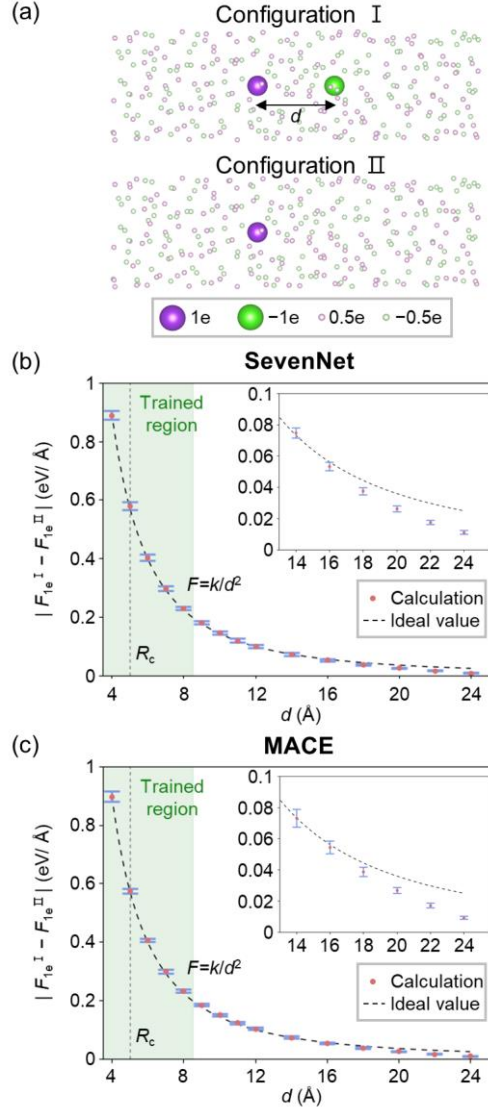


Figure 2. (a) Schematic illustration of the toy model. Difference in forces acting on 1e particle in configurations I and II calculated by (b) SevenNet and (c) MACE with five convolution layers. Ideal value is plotted as a dotted line ( $F=k/d^2$ ). Error bars represent the standard deviation of the test results. The trained regions are shaded in green. The vertical dotted line represents the cutoff ( $R_c$ ) of the trained models.

We test two types of models: the SevenNet model<sup>21</sup> based on the NequIP architecture,<sup>11</sup> and the MACE model.<sup>10</sup> The cutoff is set to 5 Å, and the number of convolutions is 5, making these models valid up to 25 Å. To assess their extrapolation ability, the models are trained at  $d$  of 4, 5, 6, 7, and 8 Å, and tested by evaluating the differences in forces acting on the 1e particles between configurations I and II ( $F_{1e}^I$  and  $F_{1e}^{II}$  respectively) at  $d$  ranging from 4 to 24 Å. Note that the ideal

value corresponds to  $k/d^2$  ( $k$ : Coulomb constant). Figures 2b,c show the results for SevenNet and MACE, respectively, both of which successfully predict  $F_{1e}^I - F_{1e}^{II}$  in both the in-distribution and out-of-distribution regions. This extrapolation behavior indicates that both models accurately learn the functional form of Coulomb interactions.

Although the predictions agree with the reference points in most parts, we observe that the predictions slightly deviate above  $\sim 20 \text{ \AA}$  (the region of the last convolution layer) in both models, as shown in the insets of Figures 2b,c. To verify whether this error in the last convolution region appears with a different number of convolution layers, we perform the same test with the models with 3 convolution layers, as shown in Figures 3a,b for SevenNet and MACE, respectively. We also observe that the accuracy of the model slightly decreases at distances of 13 and 14  $\text{\AA}$ . To systematically analyze this trend, we plot the relative error value (RMSE divided by the absolute value of  $|F_{1e}^I - F_{1e}^{II}|$ ) for SevenNet and MACE in Figures 3c,d, respectively. The normalized standard deviation (standard deviation divided by the absolute value of  $|F_{1e}^I - F_{1e}^{II}|$ ) of both models is shown in Figures 3e,f. The relative error and the normalized standard deviation show a similar trend in both models; these values increase as distance increases, especially in the last convolution layer region (3 layers: 10~15  $\text{\AA}$ , and 5 layers: 20~25  $\text{\AA}$ ). Given that MACE employs general high-order-body interaction terms (in this study, up to four-body terms) yet exhibits similar error behavior to SevenNet, it can be inferred that the error in the last convolution layer region stems from the message-passing algorithm itself. Furthermore, it can be seen that the standard deviation of the 3-layer model is higher than that of the 5-layer model at the same  $d$ . This indicates that increasing the number of convolution layers not only extends the effective cutoff distance, but also improves accuracy within regions affected by fewer convolution layers.



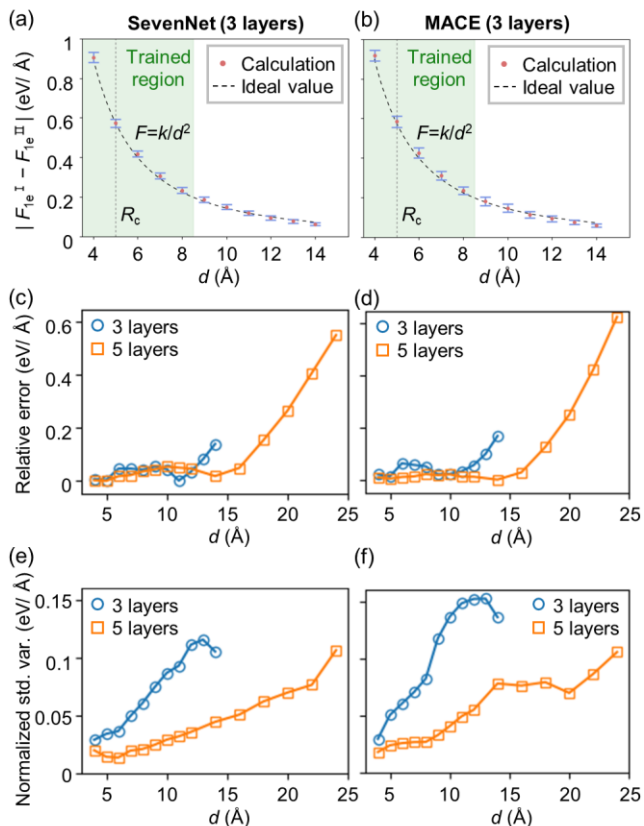


Figure 3. Difference in forces acting on a 1e particle in configurations I and II calculated by (a) SevenNet and (b) MACE with three convolution layers. Relative error values (RMSE divided the absolute value of  $|F_{1e}^I - F_{1e}^{II}|$ ) calculated by (c) SevenNet and (d) MACE as a function of  $d$ . Normalized standard variation (standard deviation divided the absolute value of  $|F_{1e}^I - F_{1e}^{II}|$ ) calculated by (e) SevenNet and (f) MACE as a function of  $d$ .

To gain insight into how GNN-IPs learn electrostatic interactions, we identify how electrostatic energies are stored in the form of atomic energy. Figures 4a,b show the atomic energy differences for the 1e particle between configuration I and II ( $E_{1e}^I$  and  $E_{1e}^{II}$ , respectively) for interpolation and extrapolation test sets, respectively. (The interpolation model is trained at  $d$  of 4, 6, 8, 10, and 12 Å.) The dotted line plots  $k/d$ , corresponding to the pairwise electrostatic energy exerted on the 1e particle by the  $-1e$  particle. The values of  $E_{1e}^I - E_{1e}^{II}$  values are significantly smaller than the pairwise electrostatic energy, which indicates that electrostatic energy between an atom pair is

distributed among neighboring atoms rather than being localized solely within the two atoms involved. This provides flexibility in the capability of MLPs to describe non-local interactions, which might help avoid contradictory scenarios arising from the non-linearity of the Coulomb interaction, as shown in Figure 1a.

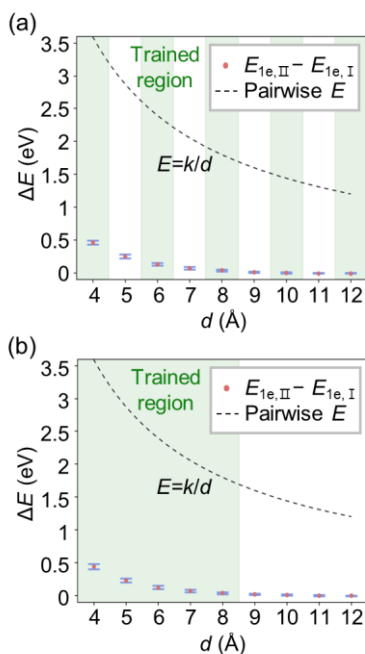


Figure 4. Difference in atomic energy of 1e particle in configuration I and II for (a) interpolation test set and (b), extrapolation test set. The absolute value of pairwise electrostatic energy between 1e and  $-1e$  ( $E=k/d$ ) is plotted in the dotted line. Error bars represent the standard deviations of the test results.

One might assume that this scenario arises from the ad hoc atomic energy mapping, where atomic energies are inaccurately mapped while total energies are trained accurately.<sup>5</sup> However, we argue against this being a case of ad hoc mapping, evidenced by the low standard deviation in  $E_{1e,I} - E_{1e,II}$  values across varying configurations (Figures 4a,b), small total-energy errors for test structures (MAE=2.4 meV/atom), and consistent results from independently trained models (interpolation and extrapolation models).

The previous example demonstrates that the GNN-IPs can learn Coulomb interactions among ideal point charges. However, it remains questionable whether GNN-IPs are capable of capturing non-local interactions in more realistic PES described by DFT, which include a wider range of interactions in addition to Coulomb interactions. To test this, we use the model system shown in Figure 5a: a SevenNet model is trained on the NVT molecular dynamics (MD) trajectories on the supercell of crystalline SrO. The trained model is tested on the structures where the center part (the atoms closer by  $R_{\text{fix}}$  to the center atom) of the cell is fixed to the crystalline structure, and the rest of the part is free to move.

Figure 5b shows the forces calculated by DFT and MLIP on the center atom under the configurations generated with  $5.82 \text{ \AA}$  of  $R_{\text{fix}}$ . The typical cutoff is  $5.5 \sim 6.0 \text{ \AA}$ , so the force should be zero when the MLIP is trained with local descriptor-based models. On the other hand, the force obtained by DFT (blue line) is not zero but oscillates up to  $\sim 0.6 \text{ eV/\AA}$ . The force values calculated by MLIP (orange line) are in good agreement with the DFT (error: green line), indicating that it learns the non-local interactions arising from beyond the cutoff distance. Given that the disordered geometries at the non-local region are not included in the training set but are well predicted by the MLIP, it indicates that the interactions are primarily derived from Coulomb interactions, which the MLIP predicts accurately. Note that the local vibrations included in the training MD trajectories of crystalline structures cause deviations in distance, enabling the MLIP to learn Coulomb interactions and make predictions even for untrained distances, as discussed in the previous subsection.

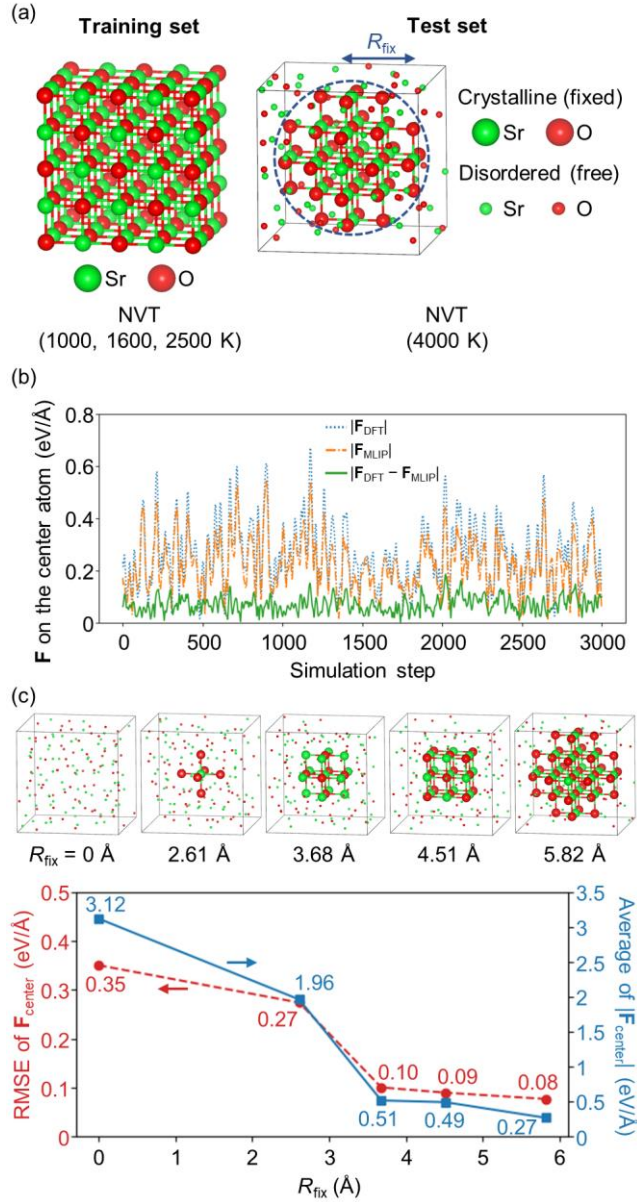


Figure 5. (a) Atomic structures of the training and test sets of the SrO system. In the test structures, the atomic structures inside  $R_{\text{fix}}$  are fixed during the MD simulations. (b) Force values of the centered atom ( $\mathbf{F}_{\text{center}}$ ) calculated by DFT and SevenNet, when  $R_{\text{fix}} = 5.82 \text{ \AA}$ . (c) Upper: the snapshots of MD simulations with various  $R_{\text{fix}}$ . Lower: RMSE and root mean average of absolute value of  $\mathbf{F}_{\text{center}}$  as a function of  $R_{\text{fix}}$ .

Figure 5c illustrates the change of root-mean-square error (RMSE) and the average force values as a function of  $R_{\text{fix}}$ . While the average absolute force value increases from  $5.82 \text{ \AA}$  to  $3.68 \text{ \AA}$ , the RMSE value remains similar. When  $R_{\text{fix}}$  becomes  $2.61 \text{ \AA}$ , both the error value and the absolute force value suddenly increase. This sudden increase supports the conclusion that force values for

$R_{\text{fix}}$  larger than 3.68 Å originate from non-local Coulomb interactions, while local interactions become significant for  $R_{\text{fix}}$  smaller than 2.61 Å, the region influenced by the training configurations.

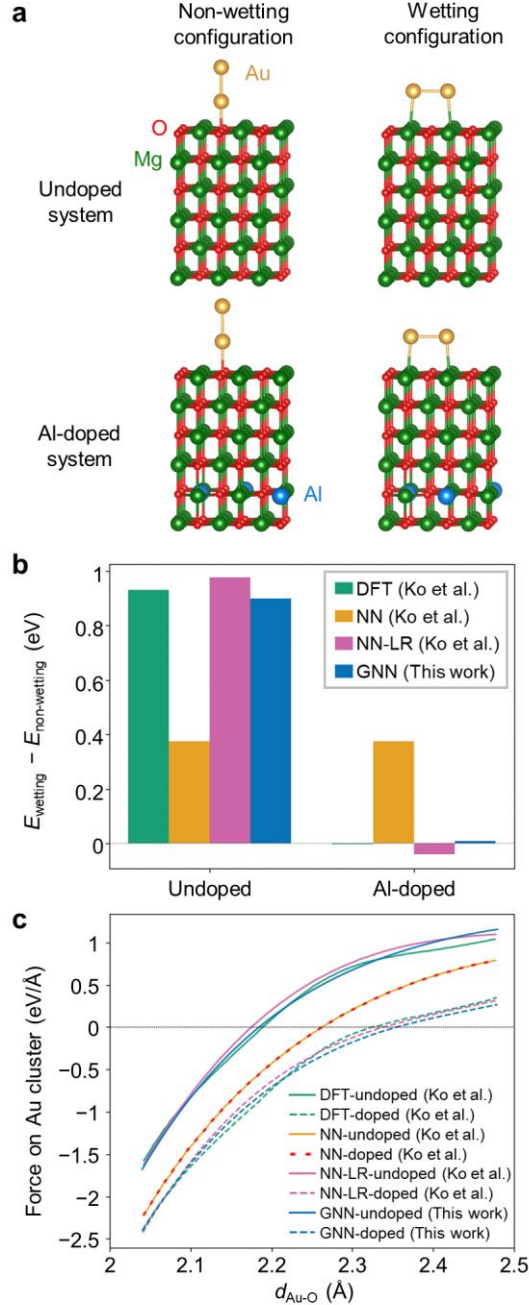


Figure 6. (a) Atomic configurations of Au<sub>2</sub> clusters in non-wetting and wetting configurations on undoped and Al-doped MgO, respectively. (b) Energy differences between wetting and non-wetting configurations as calculated by DFT, neural network (NN) potential, NN potential with long-range corrections (NN-LR), and graph neural network (GNN) potential. (c) Sum of forces acting on the Au<sub>2</sub> cluster as a function of the distance between lower Au atom and the nearest O atom in the non-wetting configuration. Results of DFT, NN, and NN-LR are extracted from ref. <sup>9</sup>.

In the previous example, the charges of the atoms do not significantly vary because SrO is an ionic material. Therefore, it is necessary to verify whether the GNN-IP can accurately capture non-local interactions in systems where the charge values change. To test this, we use a model system consisting of Au<sub>2</sub> clusters on MgO and Al-doped MgO supports (Figure 6a), as studied in ref. <sup>9</sup>. In this system, the relative energies between wetting and non-wetting configurations change in the case of Al doping, because this alters the charge value of Au<sub>2</sub> clusters due to the charge transfer from Al to Au<sub>2</sub>. In all test simulations, the atomic geometries of the supports remain fixed, thus maintaining identical local configurations around the Au<sub>2</sub> clusters. Therefore, we rule out the possibility that the MLIP identifies the energy difference from geometric differences, instead of purely inferring the effect of charge transfer from Al to Au<sub>2</sub> on the PES of the Au cluster.

Figure 6b illustrates the energy differences between the wetting and non-wetting configurations ( $E_{\text{wetting}} - E_{\text{non-wetting}}$ ) for both the MgO and Al-doped MgO systems. The Behler-Parrinello type neural network (NN) potential model<sup>2</sup> yields identical energies for both systems, because it fails to distinguish geometric difference beyond the cutoff. The NN model with long-range corrections (NN-LR) offers a more accurate prediction when compared to DFT results, as detailed in ref. <sup>9</sup>. This work finds that the GNN-IP (with cutoff distance of 6 Å) trained with SevenNet model (4 convolution layers) accurately predicts the energy differences between non-wetting and wetting configurations, with the slightly smaller error than NN-LR model.

The PES of the Au cluster is further explored in Figure 6c, which depicts the forces acting on the Au<sub>2</sub> cluster in a non-wetting configuration. This analysis is conducted while systematically varying the positions of the Au<sub>2</sub> clusters, keeping the distance between Au atoms fixed at their equilibrium position. The sum of forces on Au atoms is plotted as a function of the distance

between the lower Au atom and the nearest O atom. The trained SevenNet model successfully replicates the PES of the Au clusters on both MgO and Al-doped MgO supports, demonstrating accuracy comparable to the NN-LR model.

We also want to mention that the trained model consists of a 6 Å cutoff with 4 convolution layers. In principle, since the  $z$ -coordinate difference between Al and Au<sub>2</sub> is about 12 Å, only 3 convolution layers should be sufficient to convey information from Al to the Au<sub>2</sub> cluster. However, using this setting,  $E_{\text{wetting}} - E_{\text{non-wetting}}$  of the pure and Al-doped cases are 0.721 and 0.141 eV, respectively, which is much less accurate than the case with 4 convolution layers. This indicates that one more layer to the minimum number of layers to convey information is required to accurately describe the interaction, which is also in agreement with the toy model case described in the previous section. This might be attributed to the insufficiency of the message-passing algorithm in fully representing the accurate PES of non-local interactions.

## 2.2. Extrapolation capability of GNN-IPs

In the previous section, we prove that GNN-IPs learn non-local electrostatic interactions accurately enough to extrapolate to untrained configurations. Here, we provide a theoretical explanation for the origin of the extrapolation behavior of GNN-IPs, based on their capability to learn non-local interactions combined with their embedding characteristics.

In ref. <sup>5</sup>, it is demonstrated that the atomic energy learned from MLIPs ( $E_{\text{at},i}$ ,  $i$ : atomic index) can be divided into three terms; kinetic energy ( $E_{\text{kin},i}$ ), exchange-correlation energy ( $E_{\text{XC},i}$ ), and Coulomb energy ( $E_{\text{Coul},i}$ ):

$$E_{\text{at},i} = E_{\text{kin},i} + E_{\text{XC},i} + E_{\text{Coul},i}. \quad (1)$$

These terms are defined as follows:

$$E_{\text{kin},i} = -\frac{1}{2} \int \nabla_{\mathbf{r}}^2 \rho_{\text{at},i}(\mathbf{r}, \mathbf{r}')|_{\mathbf{r}=\mathbf{r}'} d\mathbf{r}', \quad (2)$$

$$E_{\text{XC},i} = \int \rho_i(\mathbf{r}) \varepsilon_{\text{XC}}(\rho_i(\mathbf{r}), \nabla \rho_i(\mathbf{r})) d\mathbf{r}, \quad (3)$$

$$E_{\text{Coul},i} = \frac{1}{2} \sum_{j \neq i} \frac{\rho_{\text{tot},i}(\mathbf{r}) \rho_{\text{tot},j}(\mathbf{r}')}{|\mathbf{r} - \mathbf{r}'|} d\mathbf{r} d\mathbf{r}' + \frac{1}{2} \int \frac{\rho_i(\mathbf{r}) \rho_i(\mathbf{r}')}{|\mathbf{r} - \mathbf{r}'|} d\mathbf{r} d\mathbf{r}' - \frac{1}{2} \int \frac{q_i \rho_i(\mathbf{r})}{|\mathbf{r} - \mathbf{r}_i|} d\mathbf{r}, \quad (4)$$

where,  $\rho_i$  represents the electron density within the partitioned cells (e.g. Voronoi tessellation) around atom  $i$ . The atomic density matrix ( $\rho_{\text{at},i}$ ) and total charge density ( $\rho_{\text{tot},i}$ ) are defined as follows:

$$\rho_{\text{at},i}(\mathbf{r}, \mathbf{r}') = \rho_{ii}(\mathbf{r}, \mathbf{r}') + \frac{1}{2} \sum_{j \neq i}^{\mathbf{r}_{ij} < R_c^{\text{kin}}} \rho_{ij}(\mathbf{r}, \mathbf{r}'), \quad (5)$$

$$\rho_{\text{tot},i}(\mathbf{r}) = q_i \delta(\mathbf{r} - \mathbf{r}') - \rho_i(\mathbf{r}). \quad (6)$$

$R_c^{\text{kin}}$  is the cutoff distance for kinetic energy. On the other hand, in the previous section, we show that the  $E_{\text{Coul},i}$  learned from GNN-IPs does not only include the sum of pairwise interactions involving  $i$ , but also includes a fraction of interactions between atoms around  $i$  (Figure 3).

Therefore,  $E_{\text{Coul},i}$  can be expressed as follows:

$$E_{\text{Coul},i} = \frac{1}{2} \sum_{k \neq j}^{\mathbf{r}_{ij}, \mathbf{r}_{ik} < R_c^{\text{Coul}}} w_{ikj} \frac{\rho_{\text{tot},k}(\mathbf{r}) \rho_{\text{tot},j}(\mathbf{r}')}{|\mathbf{r} - \mathbf{r}'|} d\mathbf{r} d\mathbf{r}' + \frac{1}{2} \int \frac{\rho_i(\mathbf{r}) \rho_i(\mathbf{r}')}{|\mathbf{r} - \mathbf{r}'|} d\mathbf{r} d\mathbf{r}' - \frac{1}{2} \int \frac{q_i \rho_i(\mathbf{r})}{|\mathbf{r} - \mathbf{r}_i|} d\mathbf{r}, \quad (7)$$

where  $R_c^{\text{Coul}}$  is the cutoff distance for a Coulomb interaction and  $w_{ikj}$  is the contribution of the electrostatic energy between  $k$  and  $j$  to the atomic energy of  $i$ . The sum of  $w_{ikj}$  over index  $i$  is 1.



Since  $E_{XC,i}$  is defined locally and  $E_{kin,i}$  often decays within a reasonable cutoff distance (further discussed in the next subsection), these terms can be classified as local terms. We further divide  $E_{Coul,i}$  into local and non-local terms:

$$E_{Coul,i} = E_{Coul,i}^{\text{non-local}} + E_{Coul,i}^{\text{local}}, \quad (8)$$

where each term is expressed as follows:

$$E_{Coul,i}^{\text{local}} = \frac{1}{2} \int \frac{\rho_i(\mathbf{r})\rho_i(\mathbf{r}')}{|\mathbf{r} - \mathbf{r}'|} d\mathbf{r}d\mathbf{r}' - \frac{1}{2} \int \frac{q_i\rho_i(\mathbf{r})}{|\mathbf{r} - \mathbf{r}_i|} d\mathbf{r}, \quad (9)$$

$$E_{Coul,i}^{\text{non-local}} = \frac{1}{2} \sum_{k \neq j}^{\mathbf{r}_{ij}, \mathbf{r}_{ik} < R_c^{\text{Coul}}} w_{ikj} \frac{\rho_{\text{tot},k}(\mathbf{r})\rho_{\text{tot},j}(\mathbf{r}')}{|\mathbf{r} - \mathbf{r}'|} d\mathbf{r}d\mathbf{r}'. \quad (10)$$

$E_{Coul,i}^{\text{non-local}}$  can often be approximated in a simple form, such as the pairwise interaction of charges distributed in a Gaussian shape around atoms.<sup>9</sup> Therefore, if a GNN-IP model is capable of predicting total charge values of atoms, this term can be accurately learned from a small dataset, such as distorted crystal structures (NVT MD) as shown in the previous section. In addition, the effective cutoff is extended by the message-passing algorithm, allowing unscreened non-local interactions to be learned by GNN models.

We expect that the short-range terms,  $E_{Coul,i}^{\text{local}}$ ,  $E_{kin,i}$ , and  $E_{XC,i}$  are difficult to extrapolate to untrained configurations due to the complexity of quantum mechanical PES. Even so, the GNN-IPs utilize embedding methods, so the knowledge of local structures learned from one composition can be transferred to other compositions. This is because all elements share the same networks and differ only by trainable embedding vectors. Therefore, if the GNN-IPs are trained on a large database, they would learn the local energy terms of trained configurations but in untrained compositions.

Overall, the short-range terms are interpolated in the configuration space and extrapolated in the compositional space and the non-local terms are extrapolated in the configuration space. This indicates that GNN-IPs can describe untrained structures if their local structures are included in the training data. This explains how GNN-IPs accurately describe untrained structures.

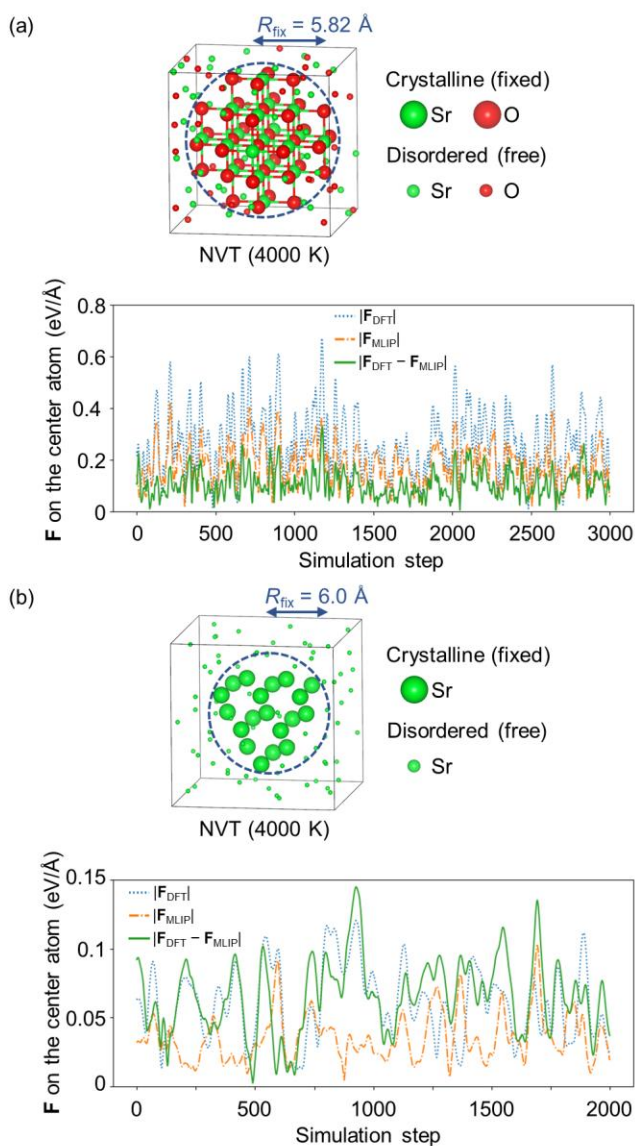


Figure 7. Atomic structures and force values of the centered atom calculated by DFT and SevenNet-0 for (a) SrO and (b) Sr. In the test structures, the atomic structures inside  $R_{\text{fix}}$  are fixed during the MD simulations.

In UIP models such as MACE-MP-0 and SevenNet-0, non-local Coulomb interactions can be effectively extrapolated to diverse materials by learning the relaxation trajectories of crystal structures in the Materials Project database. We perform numerical experiments with SevenNet-0 to confirm this hypothesis. Figure 7a shows the force values of the centered atom computed by DFT and SevenNet-0, and the RMSE values of the SrO crystal/disorder simulation trajectory, as described in Figure 5a. The average RMSE is  $0.119 \text{ eV/\AA}$ , which is slightly larger than the value shown in Figure 5c ( $0.076 \text{ eV/\AA}$ ). In addition, the overall trend in SevenNet-0 values systematically aligns with the reference DFT data. Therefore, this indicates that SevenNet-0 learned the non-local Coulomb interaction with reasonable accuracy.

We also assess the contribution of the kinetic energy term by utilizing the Sr system, as shown in Figure 7b. This material is unary and metallic, so we can assume that the electrostatic interaction beyond the cutoff is mostly screened, and the force applied to the center atom corresponds to the kinetic energy term. The graph in Figure 7b shows that the force values have an average value of  $0.066 \text{ eV/\AA}$ . SevenNet-0 does not accurately predict these force values, indicating that the kinetic energy contribution is not extrapolated. Even so, the force value is less than the typical force resolution of DFT calculations,  $0.1 \text{ eV/\AA}$ , so we expect that this will not introduce significant errors in typical simulations.

### **3. DISCUSSION**

#### **3.1. Performance of UIPs**

According to the theory suggested here, increasing the number of layers enhances the ability to extrapolate non-local electrostatic interactions, thereby improving the extrapolation capability. This might provide insights into the relative performance between SevenNet-0<sup>21</sup> and MACE-MP-

0,<sup>20</sup> the top two open-source models in the Matbench discovery benchmark platform<sup>24</sup> (<https://matbench-discovery.materialsproject.org/>, accessed 2024-07-30). SevenNet-0 shows better performance than MACE-MP-0, even though SevenNet-0 contains fewer parameters (842.4K) compared to MACE-MP-0 (4.7M) and uses the same size of training data (146K). This likely originates from the larger number of convolution layers in SevenNet-0 (five layers) compared to MACE-MP-0 (two layers), suggesting that the number of convolution layers is an important factor in the extrapolation capability. This is further supported from the fact that MACE-MP-0 even uses a higher-level message-passing algorithm compared to SevenNet-0, including many-body order message terms (in MACE-MP-0, up to 4-body terms), and utilizes a higher order of spherical expansion ( $l_{\max} = 3$ ) compared to SevenNet-0 ( $l_{\max} = 2$ ). However, we also note that the difference in self-connection methods can affect extrapolation performance, as suggested in ref. <sup>21</sup>.

Here, we focus solely on the non-local interaction term learned from the message-passing algorithm and do not specifically delve into the extrapolation capability of local terms. We anticipate that local terms are interpolated in the configuration space by embedding characteristics, although the precise interpolation ability of GNN-IP models remains unclear. Therefore, systematic methods for numerical experiments and analysis techniques, such as Uniform Manifold Approximation Projection (UMAP)<sup>25</sup> as used in ref. <sup>20</sup>, would need to be further developed.

### 3.2. Fundamental error in local MLIPs

We want to mention the typical training error values in local descriptor-based models. As shown in Figures 5,7, the magnitudes of the non-local interaction terms (0.27 eV/Å in the case of SrO) can be larger than the typical error range of DFT calculations, 0.1 eV/Å. The typical force error

values in descriptor-based models are about 0.1 to 0.3 eV/Å (for instance, refs. <sup>26-28</sup>), and the error can even reach about 0.5 eV/Å when dealing with ionic disordered structures (for instance, refs. <sup>29,30</sup>). Large parts of these error values correspond to a fundamental limit that cannot be further reduced, rather than errors from the insufficient fitting of machine learning models, given the non-local forces in DFT calculations identified in this study. Note that the error values can be less than 0.1 eV/Å when the structure is not significantly deviated from the equilibrium crystal structures, even if they contain ionic characteristics (for instance, refs. <sup>31,32</sup>). Systematic investigations into the fundamental errors arising from non-local interactions in more diverse material groups will be further studied in future works. Unlike forces, the energy errors are often minimized to a few meV/atom, which is smaller than the typical DFT error, 10 meV/atom. This might be attributed to the electrostatic interactions being averaged out and arbitrarily allocated to the elements, as confirmed in refs. <sup>5,6</sup>.

### **3.3. Applicability of GNN-IPs in diverse applications**

Finally, we suggest that GNN-IP models can be efficient tools for investigating systems that exhibit non-local interactions due to insufficient screening, even without explicitly implementing Coulomb interaction terms (for instance, see ref. <sup>9</sup>). However, the following considerations must be addressed for further practice: (1) The message-passing algorithm in GNN-IP models, which requires a third atom connecting two others beyond the cutoff, generally functions well in condensed matter systems where atoms are closely interconnected. Nevertheless, in sparser systems like molecular liquids, GNN-IP may encounter challenges in training the PES. (2) Technically, the evaluation of electrostatic energy in periodic systems necessitates calculations of an infinite sum across all periodic images, typically using methods like Ewald summation.

Currently, conventional GNN-IP models are not equipped to perform this calculation. Long-range electrostatic effects (greater than 20 Å) are generally diminished due to effective screening in most condensed matter systems, and the message-passing algorithm further reduces the remaining errors in the medium-range (10–20 Å) regions as shown in this work. However, careful attention is still required to accurately account for factors such as dielectric screening and the specific charge distribution of each system. As an example, we suggest that electrochemical environments, such as interfaces of catalysts in aqueous solvents and Li-ion batteries, can be target systems studied with GNN-IPs, as they have larger dielectric constants that effectively screen out long-range interactions.

#### 4. CONCLUSION

In summary, we provide a theoretical explanation for how GNN-IPs accurately predict untrained configurations. First, we prove that GNN-IPs learn non-local electrostatic interactions via the message-passing algorithm. This is tested with a toy model consisting of point charges, which verifies that GNN-IPs accurately predict Coulomb interactions over a range of distances not included in the training set. Next, we verify that electrostatic interactions can be inferred from distorted crystal structures generated by MD simulations, allowing for extrapolation to electrostatic interactions contributed by disordered structures. We also verify that electrostatic interactions can be learned in cases where charge values change due to charge transfer, by using the model system where Au<sub>2</sub> is adsorbed on undoped/doped MgO slabs. Finally, we demonstrate that the capability of learning electrostatic interactions and the embedding characteristics of GNN-IPs are the origin of their extrapolation capability. Based on this, we suggest that the number of convolution layers is a critical factor for enhancing the extrapolation capability of UIPs.

## 5. Methods

### 5.1. Toy model

The lattice dimensions of each cell are set to  $10 \times 10 \times (24+d)$  Å<sup>3</sup>, configured in a tetrahedral shape. Each cell contains one 1e and one -1e particle, where the coordinates of these particles are set at (5, 5, 12) and (5,5,12+d), respectively, along with  $120+5d$  particles each of 0.5e and -0.5e, which are randomly distributed within the simulation cell. The minimum interatomic distance cutoff for the random distribution is set at 1.5 Å. To eliminate periodic effects, 6 Å of vacuum layers are inserted in all directions, which is larger than the cutoff of 5 Å. In total, 200 structures are constructed for each  $d$  for training set. The test set is generated by the same method as for the training set.

### 5.2. SrO, Sr crystal/disorder system

All DFT calculations are performed with the VASP code,<sup>33</sup> using projector augmented-wave (PAW) pseudopotentials<sup>34</sup> and the PBE exchange–correlation functional.<sup>35</sup> For the SrO system, the training set includes computation results for a  $10.40 \times 10.40 \times 10.40$  Å<sup>3</sup> simulation cell containing 32 Sr and 32 O atoms. The test cell consists of a  $13.63 \times 13.63 \times 13.63$  Å<sup>3</sup> simulation cell with 72 Sr and 72 O atoms. NVT MD simulations are performed for 10 ps each at 1000 K, 1600 K, and 2500 K, with the training set sampled every 20 fs. For the test structures, initial test structures are generated by placing fixed crystal compositions in the middle of the cell and randomly positioning the rest of the atoms in the remaining space. MD simulations for the test set are performed for 6 ps at 4000 K. For the Sr system, the test set includes computation results for a  $17.29 \times 17.29 \times 17.29$  Å<sup>3</sup> simulation cell containing 96 Sr atoms, with the density set identical to the

Sr crystal. The simulations are performed for 5 ps at 4000 K. The cutoff energy values for SrO and Sr are set to 500 eV and 200 eV, respectively, as determined by the convergence test. A single gamma-point and a  $(1/4, 1/4, 1/4)$   $\mathbf{k}$ -point are used for training and test simulations, respectively, in the case of SrO. A single  $(1/4, 1/4, 1/4)$   $\mathbf{k}$ -point is used for Sr.

We note that the cutoff energies and  $\mathbf{k}$ -point densities used in our simulations are less accurate than those used in the Materials Project: 520 eV for the cutoff energy, and  $4 \times 4 \times 4$  and  $6 \times 6 \times 6$  gamma-centered  $\mathbf{k}$ -point meshes for SrO and Sr unit cells, respectively. Since SevenNet-0 is trained with the Materials Project database, this discrepancy might cause errors in the comparisons made in Figure 7. To check this, we perform tests using snapshots extracted from the test simulation trajectories and find that our settings cause deviations of only 0.012 eV/Å and 0.004 eV/Å for SrO and Sr, respectively, compared with the Materials Project settings ( $\mathbf{k}$ -point meshes are reduced to  $2 \times 2 \times 2$ , and the cutoff is set to 520 eV).

### 5.3. Au-MgO and Au/Al-MgO system

We employ the same training set and test system as utilized in ref. <sup>9</sup>. For the training set, it is stated that random displacements are applied to the configurations in the trajectory shown in Figure 2c, with a standard deviation of 0.02 Å for the substrate atoms and 0.1 Å for the gold atoms. Half of the training set corresponds to the undoped substrate, and the other half corresponds to the doped substrate. For each substrate configuration, half of the samples were generated with the Au<sub>2</sub> cluster in its wetting configuration, while the remaining half featured the cluster in its non-wetting configuration.

### 5.4. Machine-learned interatomic potentials



The SevenNet code<sup>21</sup> is used with the NequIP architecture,<sup>11</sup> and the simulations are performed with the LAMMPS code.<sup>36</sup> The model designed for the point-charge system comprises 5 convolution layers, with a maximum rotation order ( $l_{\max}$ ) of 3 and 32 features for each rotation order. The model for the SrO system includes 3 convolution layers, with a  $l_{\max}$  of 3. The model for the Au-MgO system includes 4 convolution layers, with a  $l_{\max}$  of 2 and 16 features for each rotation order. The cutoff radius of the toy model, SrO system, and Au-MgO system are set to 5, 5, and 6 Å, respectively. For all models, the invariant radial networks utilize a trainable Bessel basis of size 8 and consist of two hidden layers with 64 nodes each, featuring SiLU nonlinearities between the layers. The train/validation sets are split by the ratio of 9:1. For the MACE code, we use the similar settings as in SevenNet, except for using a correlation order of 3. All input files are publicly available at <https://doi.org/10.6084/m9.figshare.26496160.v3>.<sup>37</sup>

## 5.5. Visualization of atomic structures

All atomic configurations in this paper are drawn with VESTA code.<sup>38</sup>

## Data availability

The codes for training MLIPs, SevenNet and MACE, are open-source, and the links can be found in the original papers.<sup>10,21</sup> The training sets, test sets, input files, and the trained models are provided at <https://doi.org/10.6084/m9.figshare.26496160.v3>.<sup>37</sup> The training set for the Au-MgO system is available in the repository distributed by the previous study of Ko et al.<sup>39</sup>

## References

- (1) Unke, O. T.; Chmiela, S.; Sauceda, H. E.; Gastegger, M.; Poltavsky, I.; Schütt, K. T.; Tkatchenko, A.; Müller, K.-R. Machine Learning Force Fields. *Chem. Rev.* **2021**, *121* (16), 10142–10186.
- (2) Behler, J.; Parrinello, M. Generalized Neural-Network Representation of High-Dimensional Potential-Energy Surfaces. *Phys. Rev. Lett.* **2007**, *98* (14), 146401.
- (3) Bartók, A. P.; Payne, M. C.; Kondor, R.; Csányi, G. Gaussian Approximation Potentials: The Accuracy of Quantum Mechanics, without the Electrons. *Phys. Rev. Lett.* **2010**, *104* (13), 136403.
- (4) Deringer, V. L.; Caro, M. A.; Csányi, G. Machine Learning Interatomic Potentials as Emerging Tools for Materials Science. *Adv. Mater.* **2019**, *31* (46), 1902765.
- (5) Yoo, D.; Lee, K.; Jeong, W.; Lee, D.; Watanabe, S.; Han, S. Atomic Energy Mapping of Neural Network Potential. *Phys. Rev. Mater.* **2019**, *3* (9), 093802.
- (6) Staacke, C. G.; Heenen, H. H.; Scheurer, C.; Csányi, G.; Reuter, K.; Margraf, J. T. On the Role of Long-Range Electrostatics in Machine-Learned Interatomic Potentials for Complex Battery Materials. *ACS Appl. Energy Mater.* **2021**, *4* (11), 12562–12569.
- (7) Anstine, D. M.; Isayev, O. Machine Learning Interatomic Potentials and Long-Range Physics. *J. Phys. Chem. A* **2023**, *127* (11), 2417–2431.
- (8) Ghasemi, S. A.; Hofstetter, A.; Saha, S.; Goedecker, S. Interatomic Potentials for Ionic Systems with Density Functional Accuracy Based on Charge Densities Obtained by a Neural Network. *Phys. Rev. B* **2015**, *92* (4), 045131.
- (9) Ko, T. W.; Finkler, J. A.; Goedecker, S.; Behler, J. A Fourth-Generation High-Dimensional Neural Network Potential with Accurate Electrostatics Including Non-Local Charge Transfer. *Nat. Commun.* **2021**, *12* (1), 398.
- (10) Batatia, I.; Kovács, D. P.; Simm, G. N. C.; Ortner, C.; Csányi, G. MACE: Higher Order Equivariant Message Passing Neural Networks for Fast and Accurate Force Fields. *arXiv* **2023**, <https://arxiv.org/abs/2206.07697> (accessed 2024-08-06).
- (11) Batzner, S.; Musaelian, A.; Sun, L.; Geiger, M.; Mailoa, J. P.; Kornbluth, M.; Molinari, N.; Smidt, T. E.; Kozinsky, B. E(3)-Equivariant Graph Neural Networks for Data-Efficient and Accurate Interatomic Potentials. *Nat. Commun.* **2022**, *13* (1), 2453.
- (12) Gasteiger, J.; Giri, S.; Margraf, J. T.; Günnemann, S. Fast and Uncertainty-Aware Directional Message Passing for Non-Equilibrium Molecules. *arXiv* **2022**, <http://arxiv.org/abs/2011.14115> (accessed 2024-08-06).
- (13) Gasteiger, J.; Becker, F.; Günnemann, S. GemNet: Universal Directional Graph Neural Networks for Molecules. *arXiv* **2022**, <http://arxiv.org/abs/2106.08903> (accessed 2024-08-06).
- (14) Bochkarev, A.; Lysogorskiy, Y.; Ortner, C.; Csányi, G.; Drautz, R. Multilayer Atomic Cluster Expansion for Semilocal Interactions. *Phys. Rev. Res.* **2022**, *4* (4), L042019.
- (15) Nigam, J.; Pozdnyakov, S.; Fraux, G.; Ceriotti, M. Unified Theory of Atom-Centered Representations and Message-Passing Machine-Learning Schemes. *J. Chem. Phys.* **2022**, *156* (20), 204115.
- (16) Jain, A.; Ong, S. P.; Hautier, G.; Chen, W.; Richards, W. D.; Dacek, S.; Cholia, S.; Gunter, D.; Skinner, D.; Ceder, G.; Persson, K. A. Commentary: The Materials Project: A Materials Genome Approach to Accelerating Materials Innovation. *APL Mater.* **2013**, *1* (1), 011002.
- (17) Takamoto, S.; Shinagawa, C.; Motoki, D.; Nakago, K.; Li, W.; Kurata, I.; Watanabe, T.; Yayama, Y.; Iriguchi, H.; Asano, Y.; Onodera, T.; Ishii, T.; Kudo, T.; Ono, H.; Sawada, R.; Ishitani, R.; Ong, M.; Yamaguchi, T.; Kataoka, T.; Hayashi, A.; Charoenphakdee, N.; Ibuka,

- T. Towards Universal Neural Network Potential for Material Discovery Applicable to Arbitrary Combination of 45 Elements. *Nat. Commun.* **2022**, *13* (1), 2991.
- (18) Chen, C.; Ong, S. P. A Universal Graph Deep Learning Interatomic Potential for the Periodic Table. *Nat. Comput. Sci.* **2022**, *2* (11), 718–728.
- (19) Deng, B.; Zhong, P.; Jun, K.; Riebesell, J.; Han, K.; Bartel, C. J.; Ceder, G. CHGNet as a Pretrained Universal Neural Network Potential for Charge-Informed Atomistic Modelling. *Nat. Mach. Intell.* **2023**, *5* (9), 1031–1041.
- (20) Batatia, I.; Benner, P.; Chiang, Y.; Elena, A. M.; Kovács, D. P.; Riebesell, J.; Advincula, X. R.; Asta, M.; Avaylon, M.; Baldwin, W. J.; Berger, F.; Bernstein, N.; Bhowmik, A.; Blau, S. M.; Cărare, V.; Darby, J. P.; De, S.; Della Pia, F.; Deringer, V. L.; Elijošius, R.; El-Machachi, Z.; Falcioni, F.; Fako, E.; Ferrari, A. C.; Genreith-Schriever, A.; George, J.; Goodall, R. E. A.; Grey, C. P.; Grigorev, P.; Han, S.; Handley, W.; Heenen, H. H.; Hermansson, K.; Holm, C.; Jaafar, J.; Hofmann, S.; Jakob, K. S.; Jung, H.; Kapil, V.; Kaplan, A. D.; Karimitari, N.; Kermode, J. R.; Kroupa, N.; Kullgren, J.; Kuner, M. C.; Kuryla, D.; Liepuoniute, G.; Margraf, J. T.; Magdău, I.-B.; Michaelides, A.; Moore, J. H.; Naik, A. A.; Niblett, S. P.; Norwood, S. W.; O'Neill, N.; Ortner, C.; Persson, K. A.; Reuter, K.; Rosen, A. S.; Schaaf, L. L.; Schran, C.; Shi, B. X.; Sivonxay, E.; Stenczel, T. K.; Svahn, V.; Sutton, C.; Swinburne, T. D.; Tilly, J.; van der Oord, C.; Varga-Umbrich, E.; Vegge, T.; Vondrák, M.; Wang, Y.; Witt, W. C.; Zills, F.; Csányi, G. A Foundation Model for Atomistic Materials Chemistry. *arXiv* **2024**, <http://arxiv.org/abs/2401.00096> (accessed 2024-08-06).
- (21) Park, Y.; Kim, J.; Hwang, S.; Han, S. Scalable Parallel Algorithm for Graph Neural Network Interatomic Potentials in Molecular Dynamics Simulations. *J. Chem. Theory Comput.* **2024**, *20* (11), 4857–4868.
- (22) Merchant, A.; Bätzner, S.; Schoenholz, S. S.; Aykol, M.; Cheon, G.; Cubuk, E. D. Scaling Deep Learning for Materials Discovery. *Nature* **2023**, *624* (7990), 80–85.
- (23) Yang, H.; Hu, C.; Zhou, Y.; Liu, X.; Shi, Y.; Li, J.; Li, G.; Chen, Z.; Chen, S.; Zeni, C.; Horton, M.; Pinsler, R.; Fowler, A.; Zügner, D.; Xie, T.; Smith, J.; Sun, L.; Wang, Q.; Kong, L.; Liu, C.; Hao, H.; Lu, Z. MatterSim: A Deep Learning Atomistic Model Across Elements, Temperatures and Pressures. *arXiv* **2024**, <http://arxiv.org/abs/2405.04967> (accessed 2024-08-06).
- (24) Riebesell, J.; Goodall, R. E. A.; Benner, P.; Chiang, Y.; Deng, B.; Lee, A. A.; Jain, A.; Persson, K. A. Matbench Discovery -- A Framework to Evaluate Machine Learning Crystal Stability Predictions. *arXiv* **2024**, <http://arxiv.org/abs/2308.14920> (accessed 2024-08-06).
- (25) McInnes, L.; Healy, J.; Melville, J. UMAP: Uniform Manifold Approximation and Projection for Dimension Reduction. *arXiv* **2020**, <http://arxiv.org/abs/1802.03426> (accessed 2024-08-06).
- (26) Jung, J.; Ju, S.; Kim, P.; Hong, D.; Jeong, W.; Lee, J.; Han, S.; Kang, S. Electrochemical Degradation of Pt<sub>3</sub>Co Nanoparticles Investigated by Off-Lattice Kinetic Monte Carlo Simulations with Machine-Learned Potentials. *ACS Catal.* **2023**, *13* (24), 16078–16087.
- (27) Kang, S.; Kim, J. K.; Kim, H.; Son, Y.-H.; Chang, J.; Kim, J.; Kim, D.-W.; Lee, J.-M.; Kwon, H. J. Local Structures of Ex-Solved Nanoparticles Identified by Machine-Learned Potentials. *Nano Lett.* **2024**, *24* (14), 4224–4232.
- (28) Lee, K.; Park, Y.; Han, S. *Ab Initio* Construction of Full Phase Diagram of MgO-CaO Eutectic System Using Neural Network Interatomic Potentials. *Phys. Rev. Mater.* **2022**, *6* (11), 113802.

- (29) Hwang, S.; Jung, J.; Hong, C.; Jeong, W.; Kang, S.; Han, S. Stability and Equilibrium Structures of Unknown Ternary Metal Oxides Explored by Machine-Learned Potentials. *J. Am. Chem. Soc.* **2023**, *145* (35), 19378–19386.
- (30) Kang, S.; Jeong, W.; Hong, C.; Hwang, S.; Yoon, Y.; Han, S. Accelerated Identification of Equilibrium Structures of Multicomponent Inorganic Crystals Using Machine Learning Potentials. *npj Comput. Mater.* **2022**, *8* (1), 108.
- (31) Kang, S.; Han, S.; Kang, Y. First-Principles Calculations of Luminescence Spectra of Real-Scale Quantum Dots. *ACS Mater. Au* **2022**, *2* (2), 103–109.
- (32) Artrith, N.; Urban, A. An Implementation of Artificial Neural-Network Potentials for Atomistic Materials Simulations: Performance for TiO<sub>2</sub>. *Comput. Mater. Sci.* **2016**, *114*, 135–150.
- (33) Kresse, G.; Furthmüller, J. Efficiency of Ab-Initio Total Energy Calculations for Metals and Semiconductors Using a Plane-Wave Basis Set. *Comput. Mater. Sci.* **1996**, *6* (1), 15–50.
- (34) Blöchl, P. E. Projector Augmented-Wave Method. *Phys. Rev. B* **1994**, *50* (24), 17953–17979.
- (35) Perdew, J. P.; Burke, K.; Ernzerhof, M. Generalized Gradient Approximation Made Simple. *Phys. Rev. Lett.* **1996**, *77* (18), 3865–3868.
- (36) Plimpton, S. Fast Parallel Algorithm for Short-Range Molecular Dynamics. *J. Comput. Phys.* **1995**, *117* (1), 1–19.
- (37) Kang, S. How Graph Neural Network Interatomic Potentials Extrapolate: Role of the message-passing algorithm, **2024**. <https://doi.org/10.6084/m9.figshare.26496160.v3>.
- (38) Momma, K.; Izumi, F. VESTA 3 for Three-Dimensional Visualization of Crystal, Volumetric and Morphology Data. *J. Appl. Crystallogr.* **2011**, *44* (6), 1272–1276.
- (39) Ko, T. W.; Finkler, J. A.; Goedecker, S.; Behler, J. A Fourth-Generation High-Dimensional Neural Network Potential with Accurate Electrostatics Including Non-Local Charge Transfer, **2020**. <https://doi.org/10.24435/materialscloud:f3-yh>.

## Acknowledgements

This work was supported by the KIST Institutional Project (2E33211) and the Nano & Material Technology Development Program through the National Research Foundation of Korea (NRF) funded by Ministry of Science and ICT (RS-2024-00407995).

## Competing interests

The author declares no competing interests.

## Table of Contents

